

## Determination of Absolute Configuration of Chiral Hemicage Metal Complexes Using Time-Dependent Density Functional Theory

Frederick J. Coughlin, Karl D. Oyler, Robert A. Pascal, Jr., and Stefan Bernhard\*

Department of Chemistry, Princeton University, Princeton, New Jersey 08544

Received September 13, 2007

Time-dependent density functional theory (TD-DFT) is applied to the UV–vis absorption and circular dichroism (CD) spectra of a series of transition metals ( $M = \text{Ru}, \text{Zn}, \text{Fe}$ ) complexed with an enantiopure hemicage ligand,  $(-)-(5R,5'R,5''R,7R,7'R,7''R,8S,8'S,8''S)-8,8',8''-[(-2,4,6\text{-trimethyl-1,3,5-benzenetriyl})\text{tris(methylene)tris(5,6,7,8-tetrahydro-6,6-dimethyl-3-(2-pyridinyl)-5,7-methanoisoquinoline (1))}]$ . The electronic spectra of the Ru and Fe complexes contain two regions, one featuring low-energy  ${}^1\text{MLCT}$  transitions and the other higher energy  ${}^1\text{LC}$  transitions; the Zn analog possesses only the  ${}^1\text{LC}$  transitions due to its filled 3d shell. TD-DFT is able to identify correctly these transitions in the spectra, as well as to reproduce experimental spectra accurately, with regard to both the transition energies and the relative intensities of the different transitions. Additionally, it is possible to use TD-DFT to assign the absolute configuration at the metal center with high confidence by matching the experimental and calculated spectra.

### Introduction

Time-dependent density functional theory (TD-DFT)<sup>1–5</sup> has become an important method for research, with a diverse range of applications, including solar cells,<sup>6</sup> nonlinear optics,<sup>7,8</sup> and DNA intercalation.<sup>9</sup> TD-DFT has been shown to be computationally efficient and gives accurate results, allowing for its use in larger systems than would be possible with ordinary *ab initio* methods. This allows for the prediction of UV–visible absorption and circular dichroism (CD, the difference in absorptivity of left and right circularly polarized light) for a wide variety of transition metal complexes.

Enantiopure transition metal complexes have found use in a wide range of areas, including enantioselective catalysis<sup>10</sup> and materials applications,<sup>11</sup> for example, as materials for chiral induction.<sup>12</sup> The resolution of racemic transition metal complexes into their optically active  $\Lambda$  and  $\Delta$  isomers can be quite difficult, requiring the use of methods such as cocrystallization with chiral auxiliaries,<sup>13</sup> chromatographic resolution, or synthetic predetermination.<sup>14–16</sup> Once resolved, it is important to be able to determine the absolute configuration of the complex. Crystal structures, commonly used for this purpose, can be difficult to obtain for these complexes; moreover, in some cases the conformation and configuration of these complexes can change due to metal ion lability. For this reason, alternative chiroptical techniques that are easily linked to absolute configuration would greatly assist with structural assignments.

\* To whom correspondence should be addressed. E-mail: bern@princeton.edu.

- (1) Jamorski, C.; Casida, M. E.; Salahub, D. R. *J. Chem. Phys.* **1996**, *104*, 5134.
- (2) Petersilka, M.; Gossmann, U. J.; Gross, E. K. U. *Phys. Rev. Lett.* **1996**, *76*, 1212.
- (3) Bauernschmitt, R.; Ahlrichs, R.; Hennrich, F. H.; Kappes, M. M. *J. Am. Chem. Soc.* **1998**, *120*, 5052.
- (4) Casida, M. E. *J. Chem. Phys.* **1998**, *108*, 4439.
- (5) Stratmann, R. E.; Scuseria, G. E.; Frisch, M. J. *J. Chem. Phys.* **1998**, *109*, 8218.
- (6) Nazeeruddin, M. K.; De Angelis, F.; Fantacci, S.; Selloni, A.; Viscardi, G.; Liska, P.; Ito, S.; Takeru, B.; Grätzel, M. *J. Am. Chem. Soc.* **2005**, *127*, 16835.
- (7) Gradinaru, J.; Forni, A.; Druta, V.; Tessore, F.; Zecchin, S.; Quici, S.; Garbalau, N. *Inorg. Chem.* **2007**, *46*, 884.
- (8) Karton, A.; Iron, M. A.; van der Boom, M. E.; Martin, J. M. L. *J. Phys. Chem. A* **2005**, *109*, 5454.
- (9) Fantacci, S.; De Angelis, F.; Sgamellotti, A.; Marrone, A.; Re, N. *J. Am. Chem. Soc.* **2005**, *127*, 14144.

- (10) Inoue, Y.; Ramamurthy, V. *Chiral Photochemistry*; Marcel Dekker: New York, 2004; p 261.
- (11) Mamula, O.; von Zelewsky, A. *Coord. Chem. Rev.* **2003**, *242*, 87.
- (12) Furuno, Y.; Sato, H.; Yoshida, J.; Hoshino, N.; Fukuda, Y.; Yamagishi, A. *J. Phys. Chem. B* **2007**, *11*, 521.
- (13) Sagüés, J. A. A.; Gillard, R. D.; Smalley, D. H.; Williams, P. A. *Inorg. Chim. Acta* **1980**, *43*, 211.
- (14) Oyler, K. D.; Coughlin, F. J.; Bernhard, S. *J. Am. Chem. Soc.* **2007**, *129*, 210.
- (15) Hamann, C.; von Zelewsky, A.; Neels, A.; Stoeckli-Evans, H. *J. Chem. Soc., Dalton Trans.* **2004**, 402.
- (16) Schaffner-Hamann, C.; von Zelewsky, A.; Barbieri, A.; Barigelletti, F.; Müller, G.; Riehl, J. P.; Neels, A. *J. Am. Chem. Soc.* **2004**, *126*, 9339.

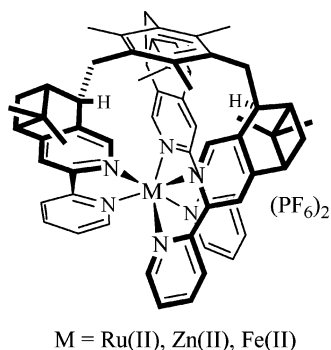


**Figure 1.** Structure of  $M(\mathbf{1})(\text{PF}_6)_2$ .

Since the discovery of circular dichroism and optical rotation in transition metal complex solutions by Cotton in the 1890s,<sup>17</sup> chiroptical properties have been a useful tool for the characterization of these compounds. CD spectra often are used only to demonstrate the presence of an excess of one enantiomer in a sample, but these spectra also contain information about the molecular configuration itself. Correlation methods<sup>18</sup> and sector rules<sup>19,20</sup> have been used to determine absolute configuration from CD spectra; however, use of these methods can be quite problematic.<sup>21,22</sup> The ability to compare these experimental spectra with spectra calculated by theoretical methods would certainly improve the accuracy of the assignments.

Although many examples exist in the literature for the calculation of CD spectra of organic molecules,<sup>23–27</sup> only recently have these methods been turned to transition metal complexes. Due to the relatively large size and electronic complexity of these compounds, common ab initio methods are not applicable. Recently, TD-DFT has been used successfully to calculate these spectra.<sup>28–31</sup>

Herein, we explore the calculated UV–vis and CD spectra of  $M(\mathbf{1})^{2+}$  (see Figure 1), where  $M = \text{Ru}, \text{Fe},$  or  $\text{Zn}$ . These molecules have been synthesized with the configurations about the metal centers predetermined by a chiral hemicage ligand, thus establishing the absolute configurations around

the metal centers. Inasmuch as the CD spectra in these molecules are determined by their absolute configurations, the ability to match calculated and experimental CD spectra can be used to assign the configuration. In contrast to their uncaged cousins, these cage molecules are substitutionally inert, allowing the coordination of metals that might otherwise be highly labile in solution (with consequent loss of stereochemical integrity). The rigid structure enhances the spectral intensity by reducing nonradiative decay and increasing quantum efficiency. Using TD-DFT, we have successfully reproduced the CD and UV–vis spectra of these complexes. This work demonstrates the ability of TD-DFT to calculate accurately the CD spectra and the absolute configuration around the metal centers for several metal complexes.

## Experimental Section

**General Methods.** Reagents were purchased from Aldrich and used as received. The synthesis and characterization of  $\Delta\text{-}[\text{Zn}(\mathbf{1})](\text{PF}_6)_2$  and  $\Delta\text{-}[\text{Ru}(\mathbf{1})](\text{PF}_6)_2$  were as previously described.<sup>14</sup> A Varian INOVA 500 MHz spectrometer was used to record <sup>1</sup>H NMR (500 MHz) and <sup>13</sup>C NMR (125 MHz) spectra. A Hewlett-Packard 5898B MS Engine was used to measure electrospray mass spectra. Elemental analyses were carried out by the University of Illinois at Urbana Champaign Microanalysis Laboratory.

$\Delta\text{-}[\text{Fe}(\mathbf{1})](\text{PF}_6)_2$ . Ligand **1** (0.050 g, 0.055 mmol) was dissolved in 100 mL of hot ethanol, and  $\text{FeNH}_4\text{SO}_4$  (0.022 g, 0.055 mmol) was added in small portions over 30 min. The red solution was heated under reflux for 3 h before removal of the solvent by rotary evaporation. The resulting dark red solid was then dissolved in 50 mL of water, and a solution of  $\text{NH}_4\text{PF}_6$  (1.00 g) in 5 mL of water was added to precipitate the iron complex as a  $\text{PF}_6^-$  salt. The compound was separated by filtration, dissolved in acetone, and filtered through a short column of aluminum oxide to remove polymeric impurities. Following evaporation of the solvent from the filtrate, recrystallization by vapor diffusion of acetonitrile and ether yielded 0.028 g (0.022 mmol, 40%) of pure product. <sup>1</sup>H NMR (500 MHz, acetone-*d*<sub>6</sub>):  $\delta$  0.27 (s, 9 H), 1.49 (s, 9 H), 2.04 (d,  $J = 10.4$  Hz, 3 H), 2.19 (s, 9 H), 2.44 (m, 3 H), 2.83 (m, 3 H), 2.96 (m, 3 H), 3.14 (m, 6 H), 3.56 (m, 3 H), 6.98 (s, 3 H), 7.19 (d,  $J = 5.5$  Hz, 3 H), 7.45 (dd,  $J = 7.8$  Hz, 5.5 Hz, 3 H), 8.17 (t,  $J = 7.8$  Hz, 3 H), 8.40 (s, 3 H), 8.65 (d,  $J = 7.8$  Hz, 3 H). <sup>13</sup>C NMR (125 MHz, acetone-*d*<sub>6</sub>):  $\delta$  17.56, 20.02, 25.55, 27.91, 35.60, 37.43, 42.52, 46.88, 48.39, 121.22, 123.61, 127.14, 134.96, 136.32, 137.24, 138.66, 152.49, 153.73, 156.72, 158.91, 160.05. MS (*m/z*, ESI): 1111 (1%,  $[\text{M} - \text{PF}_6]^+$ ), 483 (100%,  $[\text{M} - 2\text{PF}_6]^{2+}$ ). Anal. Calcd for  $\text{C}_{63}\text{H}_{66}\text{N}_6\text{Fe}(\text{PF}_6)_2 \cdot \text{H}_2\text{O}$ : C, 59.53; H, 5.35; N, 6.61. Found: C, 59.65; H, 5.22; N, 6.70.

**Photophysical Measurements.** All spectroscopic measurements were obtained from 25  $\mu\text{M}$  acetonitrile solutions as previously described.<sup>14</sup>

**Computational Details.** All density functional theory (DFT) calculations were carried out by using the GAUSSIAN 03 suite.<sup>32</sup> Ground- and excited-state geometries (both singlet and triplet) for all complexes were evaluated computationally using Becke's three-parameter exchange functional (B3)<sup>33</sup> in conjunction with the Lee, Yang, and Parr (LYP)<sup>34</sup> nonlocal functional. The default thresholds for gradient convergence with a slightly relaxed threshold for wave function convergence [SCF=(CONVER=7)] were used for all calculations. The LANL2DZ basis set was employed for all

- (17) (a) Cotton, A. C. *R. Acad. Sci.* **1885**, 120, 1044. (b) Cotton, A. *Ann. Chim. Phys.* **1896**, 8, 347.
- (18) Bijvoet, J. M.; Peerdeman, A. F.; Van Bommel, A. J. *Nature* **1951**, 168, 271.
- (19) Hawkins, C. J.; Larsen, E. *Acta Chem. Scand.* **1965**, 19, 1969.
- (20) Richardson, F. S. *J. Chem. Phys.* **1971**, 54, 2453.
- (21) Ripa, L.; Hallberg, A.; Sandstroem, J. *J. Am. Chem. Soc.* **1997**, 119, 5701.
- (22) Kuroda, R.; Saito, Y. In *Circular Dichroism. Principles and Applications*; Nakanishi, K., Berova, N., Woody, R. W., Eds.; VCH: New York, 1994; p 217.
- (23) Mori, T.; Inoue, Y.; Grimme, S. *J. Org. Chem.* **2006**, 71, 9797.
- (24) Fabian, J.; Diaz, L. A.; Seifert, G.; Niehaus, T. *THEOCHEM* **2002**, 594, 41.
- (25) McCann, D. M.; Stephens, P. J. *J. Org. Chem.* **2006**, 71, 6074.
- (26) Stephens, P. J.; McCann, D. M.; Butkus, E.; Stoncius, S.; Cheeseman, J. R.; Frisch, M. J. *J. Org. Chem.* **2004**, 69, 1948.
- (27) Autschbach, J.; Ziegler, T.; van Gisbergen, S. J. A.; Baerends, E. J. *J. Chem. Phys.* **2002**, 116, 6930–6940.
- (28) Jorge, F. E.; Autschbach, J.; Ziegler, T. *J. Am. Chem. Soc.* **2005**, 127, 975.
- (29) Mack, J.; Asano, Y.; Kobayashi, N.; Stillman, M. J. *J. Am. Chem. Soc.* **2005**, 127, 17697.
- (30) Fantacci, S.; De Angelis, F.; Selloni, A. *J. Am. Chem. Soc.* **2003**, 125, 4381.
- (31) Fantacci, S.; De Angelis, F.; Wang, J.; Bernhard, S.; Selloni, A. *J. Am. Chem. Soc.* **2004**, 126, 9715.

molecules.<sup>35</sup> Additional calculations on the Zn and Fe hemicages were performed with the 6-31G(d) basis set.<sup>36</sup> For each metal complex, time-dependent DFT (TD-DFT) calculations were performed at the optimized ground-state geometry, calculating the energy, oscillator strength, and rotatory strength for each of the 100 lowest singlet excitations. To simulate solvent effects, the TD-DFT calculations were performed using the conductor polarizable continuum model (C-PCM) present in Gaussian 03.<sup>37</sup> The geometry of the lowest triplet state was also obtained by using unrestricted B3LYP calculations. Calculation of UV-vis and CD spectra was accomplished using GaussSum 2.0.<sup>38</sup> Electronic transitions were expanded as Gaussian curves, with a fwhm (full width at half-maximum) for each peak set to 0.12 eV.

## Results and Discussion

**Ru(1)<sup>2+</sup>.** The electronic structure for the Ru(1)<sup>2+</sup> cage features electron density on two distinct  $\pi$  systems, as seen in Figure 2. The three highest occupied molecular orbitals (orbitals 248–250) are located primarily on the d orbitals of the metal center. Orbitals 246 and 247, 0.45 eV below the HOMO, are two degenerate orbitals localized on the  $\pi$  system of the phenyl cap. At 1.22 eV beneath the HOMO are three orbitals (243–245) located on the 2,2'-bipyridine  $\pi$  orbitals. Very similar orbitals are also found in the uncaged Ru(bpy)<sub>3</sub><sup>2+</sup> molecule,<sup>39</sup> at approximately the same energy gap from the HOMO, indicating that the pinene substituents do not significantly change the electronic structure. The lowest unoccupied molecular orbitals (orbitals 251–253 in the caged complex) in both Ru(1)<sup>2+</sup> and Ru(bpy)<sub>3</sub><sup>2+</sup> are localized on the  $\pi^*$  orbitals of E symmetry on the 2,2'-bipyridine ligand, located 3.37 eV above the HOMO. Above these are several orbitals on various parts of the 2,2'-bipyridine rings. Unoccupied orbitals with a strong metal 4d character are the LUMO+14 and LUMO+15 (orbitals 265 and 266), located 6.07 eV above the HOMO; these orbitals are related to the e<sub>g</sub><sup>\*</sup> orbitals in octahedral complexes.

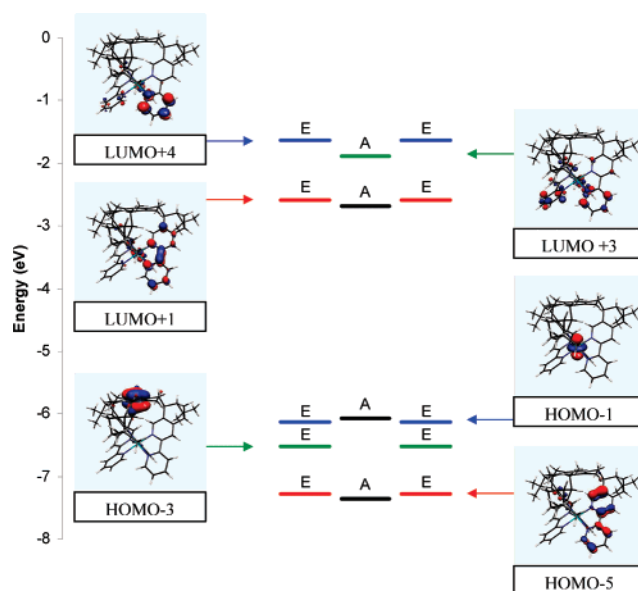


**Figure 2.** MO diagram of the C<sub>3</sub> complex  $\Delta$ -[Ru(1)]<sup>2+</sup> in CH<sub>3</sub>CN. Orbital symmetries are listed above each orbital.

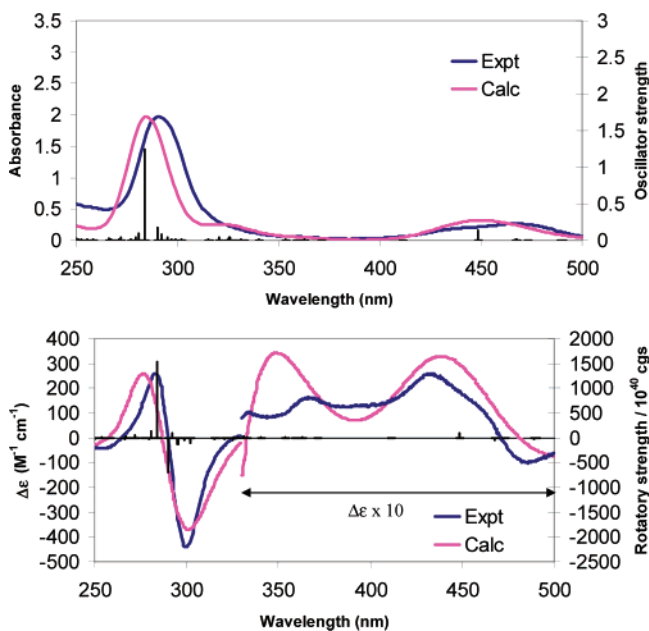


**Figure 3.** Experimental and calculated UV-vis spectra (top) and CD spectra (bottom) for  $\Delta$ -[Ru(1)]<sup>2+</sup> in CH<sub>3</sub>CN. The calculated UV-vis and CD spectra have been normalized to the maximum positive value to ease comparison of experimental and calculated data. Oscillator strengths and rotatory strengths are shown as unbroadened vertical lines.

The calculated UV-vis and CD spectra for the Ru cage are shown in Figure 3. The spectra are defined by two distinct bands. The lowest energy band, located at 448 nm, originates from a pair of <sup>1</sup>E MLCT transitions from orbitals 248 and 249 to orbitals 251–253; this is consistent with previous work describing the transitions in these compounds.<sup>40</sup> The next highest band is a <sup>1</sup>A ligand centered transition from the  $\pi$  orbitals on the 2,2'-bipyridine to the  $\pi^*$  orbitals occurring at 292 nm.

- (32) Frisch, M. J.; Trucks, G. W.; Schlegel, H. B.; Scuseria, G. E.; Robb, M. A.; Cheeseman, J. R.; Montgomery, J. A., Jr.; Vreven, T.; Kudin, K. N.; Burant, J. C.; Millam, J. M.; Iyengar, S. S.; Tomasi, J.; Barone, V.; Mennucci, B.; Cossi, M.; Scalmani, G.; Rega, N.; Petersson, G. A.; Nakatsuji, H.; Hada, M.; Ehara, M.; Toyota, K.; Fukuda, R.; Hasegawa, J.; Ishida, M.; Nakajima, T.; Honda, Y.; Kitao, O.; Nakai, H.; Klene, M.; Li, X.; Knox, J. E.; Hratchian, H. P.; Cross, J. B.; Adamo, C.; Jaramillo, J.; Gomperts, R.; Stratmann, R. E.; Yazyev, O.; Austin, A. J.; Cammi, R.; Pomelli, C.; Ochterski, J. W.; Ayala, P. Y.; Morokuma, K.; Voth, G. A.; Salvador, P.; Dannenberg, J. J.; Zakrzewski, V. G.; Dapprich, S.; Daniels, A. D.; Strain, M. C.; Farkas, O.; Malick, D. K.; Rabuck, A. D.; Raghavachari, K.; Foresman, J. B.; Ortiz, J. V.; Cui, Q.; Baboul, A. G.; Clifford, S.; Cioslowski, J.; Stefanov, B. B.; Liu, G.; Liashenko, A.; Piskorz, P.; Komaromi, I.; Martin, R. L.; Fox, D. J.; Keith, T.; Al-Laham, M. A.; Peng, C. Y.; Nanayakkara, A.; Challacombe, M.; Gill, P. M. W.; Johnson, B.; Chen, W.; Wong, M. W.; Gonzalez, C.; Pople, J. A. *Gaussian 03*; Gaussian, Inc.: Wallingford, CT, 2004.
- (33) Becke, A. D. *J. Chem. Phys.* **1993**, *98*, 5648.
- (34) (a) Lee, C.; Yang, W.; Parr, R. G. *Phys. Rev. B* **1988**, *37*, 785. (b) Miehlich, B.; Savin, A.; Stoll, H.; Preuss, H. *Chem. Phys. Lett.* **1989**, *157*, 200.
- (35) (a) Hay, P. J.; Wadt, W. R. *J. Chem. Phys.* **1985**, *82*, 299. (b) Hay, P. J.; Wadt, W. R. *J. Chem. Phys.* **1985**, *82*, 270. (c) Hay, P. J.; Wadt, W. R. *J. Chem. Phys.* **1985**, *82*, 284.
- (36) Hariharan, P. C.; Pople, J. A. *Theor. Chim. Acta* **1973**, *28*, 213.
- (37) Cossi, M.; Barone, V. *J. Chem. Phys.* **2001**, *115*, 4708.
- (38) O'Boyle, N. M. *GaussSum 2.0*; available at <http://gausssum.sf.net>, 2006.
- (39) Stoyanov, S. R.; Villegas, J. M.; Rillema, D. P. *Inorg. Chem.* **2002**, *41*, 2941.
- (40) Kalyanasundaram, K. *Photochemistry of Polypyridine and Porphyrin Complexes*; Academic Press Limited: London, 1992.

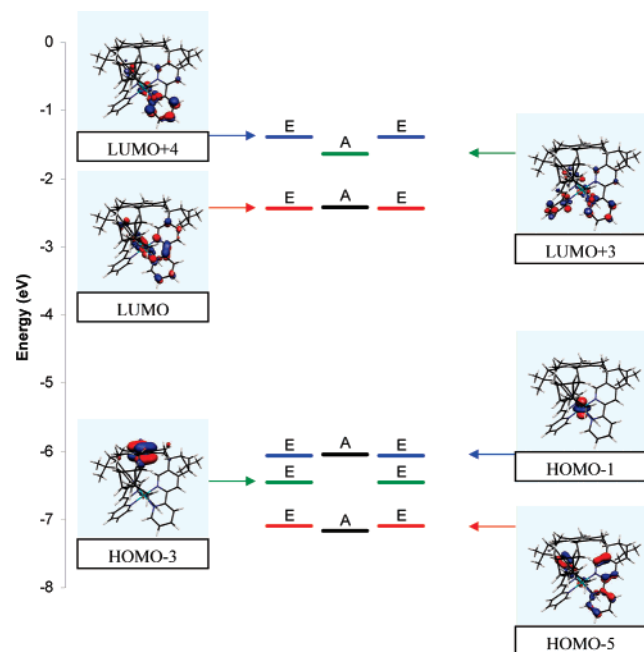


**Figure 4.** MO diagram of the  $C_3$  complex  $\Delta$ -[Fe(1)]<sup>2+</sup> in  $CH_3CN$ . Orbital symmetries are listed above each orbital.

Detailed analysis of the calculated CD spectra shows that these transitions also yield the CD bands. Strong transitions of similar magnitude but opposite sign are visible at 290 (two degenerate <sup>1</sup>E) and 283 (<sup>1</sup>A) nm; these transitions cause the dichroic effect seen near 285 nm and originate from the  $\pi$ - $\pi^*$  transitions on the 2,2'-bipyridines. The <sup>1</sup>MLCT transition at 448 nm produces a much smaller CD signal than that due to the ligand-centered transition. This smaller signal may partially result from the path traveled by the electrons during the transition. In the <sup>1</sup>LC transition, the electron moves in a helical path around the metal center, while the <sup>1</sup>MLCT transition involves the electron moving directly toward the metal center. The calculated and experimental spectra are in excellent agreement, in both the relative ordering and magnitude of the transitions as well as the signs of the Cotton effect.

**Fe(1)<sup>2+</sup>.** The electronic structure of the Fe(1)<sup>2+</sup> molecule (shown in Figure 4) also exhibits electron density on two different  $\pi$  systems. The three HOMOs (orbitals 248–250) are located on the “ $t_{2g}$ ” orbitals of the Fe. The next two degenerate orbitals (246 and 247) are located on the  $\pi$  orbitals of the cap, approximately 0.63 eV below the HOMO, followed by the degenerate  $\pi$  orbitals on the 2,2'-bipyridine rings, located 1.04 eV below the HOMO. Similarly, the LUMOs (251–253) are localized on the  $\pi^*$  orbitals of the 2,2'-bipyridine rings, with a HOMO–LUMO gap of 3.62 eV. The “ $e_g^*$ ” orbitals are located in the LUMO+10 and LUMO+11 (orbitals 261 and 262), 5.88 eV above the HOMO.

The calculated UV–vis and CD spectra for the Fe cage are shown in Figure 5. The spectra are similar in shape to those of the Ru cage; the relative ordering and magnitude of the transitions remains unchanged, with small changes in energy present. The observed difference between the experimental and calculated transition energies can be attributed

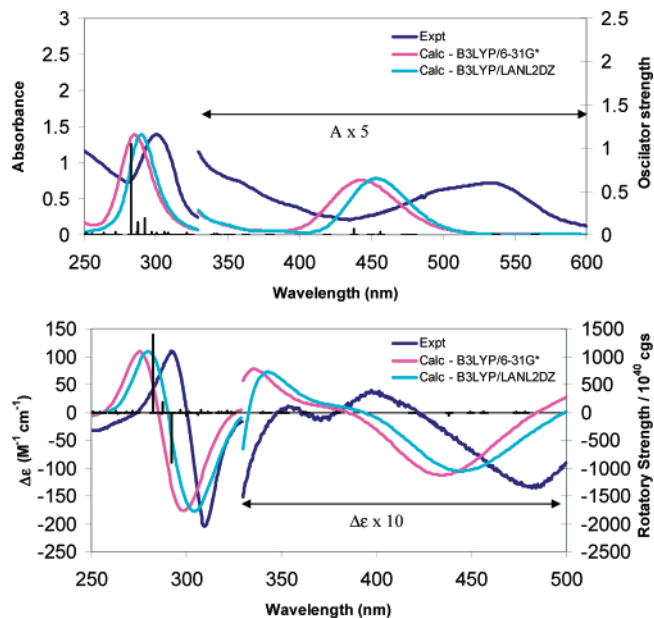


**Figure 5.** Experimental and calculated UV–vis spectra (top) and CD spectra (bottom) for  $\Delta$ -[Fe(1)]<sup>2+</sup> in  $CH_3CN$ . The calculated UV–vis and CD spectra have been normalized to the maximum positive value to ease comparison of experimental and calculated data. Oscillator strengths and rotatory strengths of the B3LYP/6-31G(d) calculation are shown as unbroadened vertical lines.

to the density functional method chosen; B3LYP and other functionals have been shown to overestimate interaction between d orbitals and ligands for 3d metal systems.<sup>41,42</sup> Changing the basis set from LANL2DZ to the 6-31G(d) basis set gave a slight improvement in the energy of the transitions in the CD spectrum while still preserving the correct ordering of the transitions. Although the calculated CD spectrum matches the experimental data, it is important to note that the low energy <sup>1</sup>MLCT transitions do not always match. Mason et al.<sup>43</sup> showed that the sign of these transitions are different in Ru(phen)<sup>2+</sup> and Fe(phen)<sup>2+</sup>, and Autschbach<sup>44</sup> showed that the choice of functional can influence the calculated sign of these transitions. In all of these cases, the high-energy  $\pi$ - $\pi^*$  transitions are correctly predicted and thus can be used with greater confidence to determine the configuration about the metal center.

**Zn(1)<sup>2+</sup>.** The calculated UV–vis and CD spectra for the Zn hemicage are shown in Figure 6. Zn<sup>2+</sup> has a filled 3d shell; as a result, the Zn(1) complex has a electronic structure significantly different from that of its Ru(II) and Fe(II) counterparts. The HOMO and HOMO-1 (orbitals 248 and 247, respectively) of this complex are doubly degenerate  $\pi$  orbitals located on the phenyl cap of the hemicage. Located 0.61 eV below these are the almost triply degenerate orbitals (orbitals 244–246) located on the  $\pi$  orbitals of the 2,2'-bipyridine rings. The doubly degenerate “ $e_g^*$ ” orbitals, 1.18 eV below the HOMO, have a mixed  $\pi$ -“ $e_g^*$ ” character (unlike Fe(1) and Ru(1), in which the “ $e_g^*$ ” orbitals were

(41) Autschbach, J.; Jorge, F. E.; Ziegler, T. *Inorg. Chem.* **2003**, *42*, 2867.

(42) Le Guennic, B.; Hieringer, W.; Görling, A.; Autschbach, J. *J. Phys. Chem. A* **2005**, *109*, 4836.

(43) McCaffery, A. J.; Mason, S. F.; Norman, B. J. *J. Chem. Soc. A* **1969**, 1428.

(44) Autschbach, J. *Coord. Chem. Rev.* **2007**, *251*, 1796.

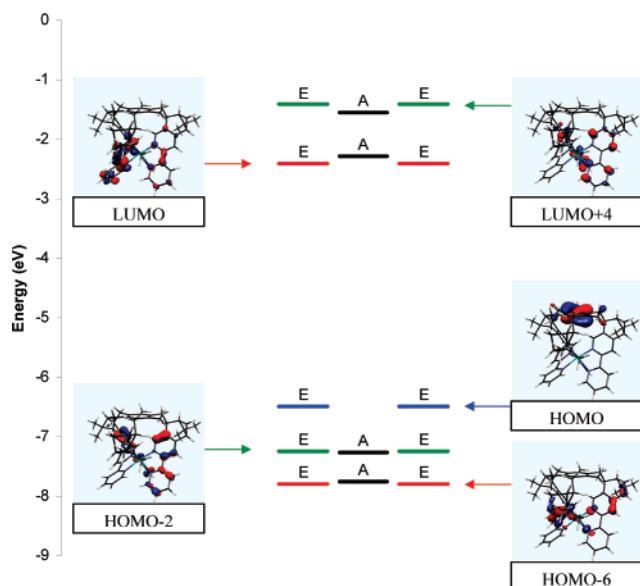


**Figure 6.** MO diagram of the  $C_3$  complex  $\Delta$ -[Zn(1)]<sup>2+</sup> in CH<sub>3</sub>CN. Orbital symmetries are listed above each orbital.

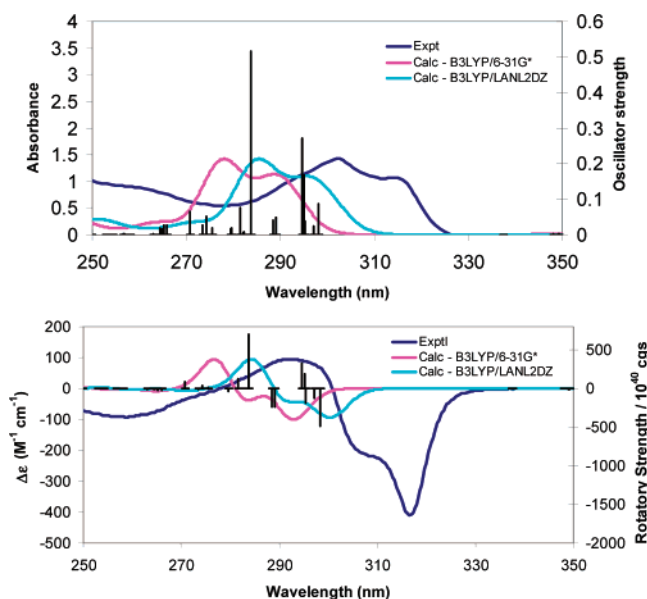


**Figure 7.** Experimental and calculated UV-vis spectra (top) and CD spectra (bottom) for  $\Delta$ -[Zn(1)]<sup>2+</sup> in CH<sub>3</sub>CN. The calculated UV-vis and CD spectra have been normalized to the maximum positive value to ease comparison of experimental and calculated data. Oscillator strengths and rotatory strengths of the B3LYP/6-31G(d) calculation are shown as unbroaderd vertical lines.

not occupied). The LUMOs (orbitals 249–251) for the Zn complex are on the  $\pi^*$  orbitals on the 2,2'-bipyridine rings, 4.04 eV above the HOMO.

The Zn(1) calculated spectra show very good agreement with experimental data, as seen in Figure 7. The lowest energy band in the spectrum originates from the  $\pi$ - $\pi^*$  transition from the 2,2'-bipyridine  $\pi$  orbitals (orbitals 245 and 246) to the LUMOs (orbitals 249 and 250). Due to the large, opposite-signed, rotatory strengths of these transitions, we see the characteristic dichroic peaks at 292 and 316 nm in the experimental CD spectrum. The calculated spectra show several  $\pi$ - $\pi^*$  transitions in that region, corresponding to several strong <sup>1</sup>A transitions at 298, 295, and 284 nm,

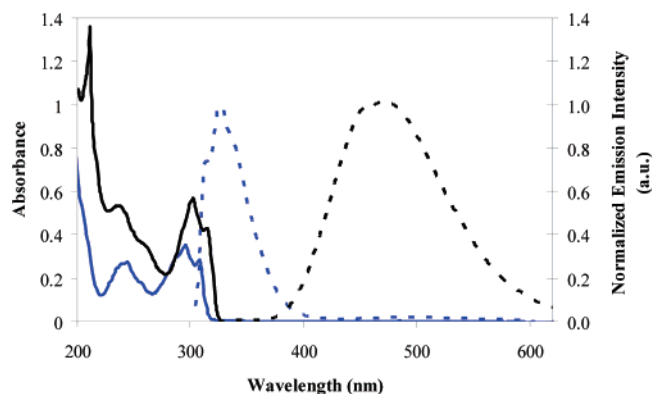


**Figure 8.** Combined absorption (solid) and emission (dashed) spectra of Zn(1)(PF<sub>6</sub>)<sub>2</sub> (black) and Zn(bpy)<sub>3</sub>(PF<sub>6</sub>)<sub>2</sub> (blue).

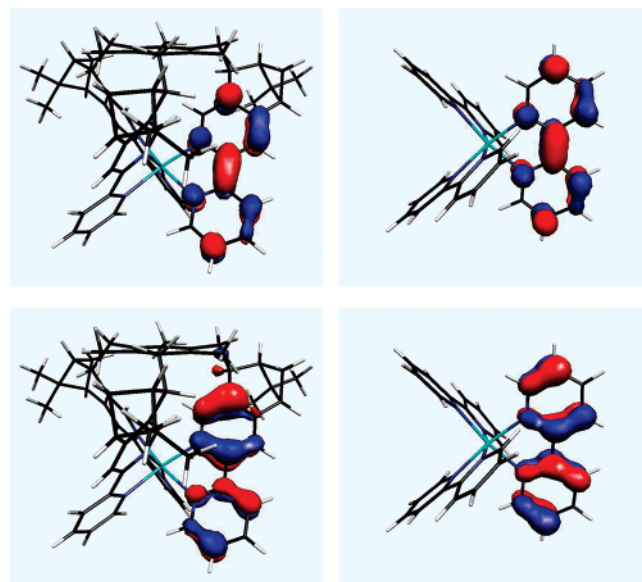


**Figure 9.** HSOMO (top) and LSOMO (bottom) for the parent Zn(bpy)<sub>3</sub><sup>2+</sup> (right) and  $\Delta$ -[Zn(1)]<sup>2+</sup> (left).

along with a pair of <sup>1</sup>E transitions at 295 nm. These transitions also lead to very strong dichroic peaks in the CD spectra. As expected, no <sup>1</sup>MLCT transitions were observed; the filled 3d orbitals are not involved in any of the ligand-centered transitions seen in the UV-vis spectra. A comparison of the experimental and calculated spectra shows remarkable agreement with only a small difference in energy that can again be contributed to HOMO-LUMO gap overestimation by the density functional calculation. Both B3LYP/LANL2DZ and B3LYP/6-31G(d) calculations correctly predict the signs, relative magnitudes, and energies of the spectra.

Very surprisingly, the Zn(1) complex exhibits phosphorescence from the lowest triplet state to the ground singlet state.<sup>14</sup> The absorption and emission spectra for these complexes are shown in Figure 8. Triplet calculations indicate that the highest singly occupied molecular orbital (HSOMO) is primarily located on the  $\pi^*$  orbitals on the 2,2'-bipyridine rings, as seen in Figure 9. Phosphorescence occurs when this electron returns to the LSOMO (the lowest singly occupied molecular orbital, localized on the  $\pi$  orbitals on the 2,2'-bipyridine rings). This is surprising when compared to the uncaged Zn(bpy)<sub>3</sub><sup>2+</sup> complex, which fluoresces when

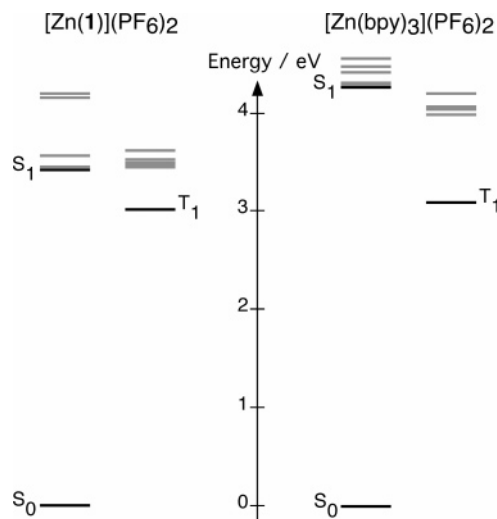


**Figure 10.** Energy diagrams of  $[\text{Zn}(\mathbf{1})](\text{PF}_6)_2$  and  $[\text{Zn}(\text{bpy})_3](\text{PF}_6)_2$  obtained through TD-DFT calculations (B3LYP/LANL2DZ) at the geometry-optimized singlet geometries. The first 10 states, some of them degenerate, are depicted for the singlet and the triplet manifold. A faster rate of intersystem crossing can be observed in the hemicage complex due to the smaller energy gap between the  $S_1$  and the  $T_1$  state. The more rigid nature of the hemicage complex as well as energetically accessible higher energy triplet states can also facilitate such a change in multiplicity.

excited. Analysis of TD-DFT calculations (as seen in Figure 10) indicates that the mesityl cap of the hemicage ligand plays an important role in facilitating intersystem crossing. The singlet–singlet TD-DFT calculations show that there are several weak transitions (transitions 1–6 in Supporting Information) at 3.42–3.54 eV corresponding to transitions from the mesityl  $\pi$  orbitals to the  $\pi^*$  orbitals on the 2,2'-bipyridine rings. Singlet–triplet TD-DFT calculations show that excited triplet states exist with similar electronic structure (aside from the difference in multiplicity) at very close energies; this greatly improves the probability of a spin flip,

leading to the observed higher rate of intersystem crossing. In contrast, the very large energy gap between the singlet–singlet and singlet–triplet energies of  $\text{Zn}(\text{bpy})_3^{2+}$  leads to a slower rate of intersystem crossing, allowing the fluorescent pathway to become dominant.

## Conclusions

We have presented TD-DFT calculations on the UV–vis and CD spectra of  $\Delta\text{-M}(\mathbf{1})$ . The low-energy part of the spectra in the Ru and Fe complexes represents HOMO-to-LUMO  $^1\text{MLCT}$  transitions, while the higher energy portion represents more intense  $^1\text{LC } \pi\text{-}\pi^*$  transitions. The Zn hemicage lacks the  $^1\text{MLCT}$  transitions due to its filled 3d shell; instead, the strong transitions are solely  $^1\text{LC}$ . TD-DFT calculations correctly identify these transitions, as well as predicting experimental UV–vis and CD spectra with accuracy. In addition, these calculations correctly predict the stereochemistry of the metal center, they correctly predict the relative size and energies of the transitions leading to the dichroic peaks caused by the  $^1\text{LC}$  transitions, and they correctly predict the sign of the  $^1\text{MLCT}$  transitions in the Ru and Fe hemicages. By matching the calculated spectra to experimental results, it is thus possible to accurately determine the absolute configurations of these complexes.

**Acknowledgment.** This work was supported by the National Science Foundation (CHE-0449755 to S.B. and CHE-0614879 to R.A.P.).

**Supporting Information Available:** Transition energies, composition, and oscillator strengths from TD-DFT calculations. This material is available free of charge via the Internet at <http://pubs.acs.org>.

IC701804K